Highly Active Pt_3Pb and Core–Shell Pt_3Pb–Pt Electrocatalysts for Formic Acid Oxidation

Yijin Kang,[†] Liang Qi,[‡] Meng Li,[§] Rosa E. Diaz,[⊥] Dong Su,[⊥] Radoslav R. Adzic,[§] Eric Stach,[⊥] Ju Li,[‡] and Christopher B. Murray[†,‡,*]

[†]Department of Chemistry, University of Pennsylvania, Philadelphia, Pennsylvania 19104, United States , [‡]Department of Materials Science and Engineering, University of Pennsylvania, Philadelphia, Pennsylvania 19104, United States , [§]Department of Chemistry, Brookhaven National Laboratory, Upton, New York 11973, United States, and [⊥]Center for Functional Nanomaterials, Brookhaven National Laboratory, Upton, New York 11973, United States

ABSTRACT

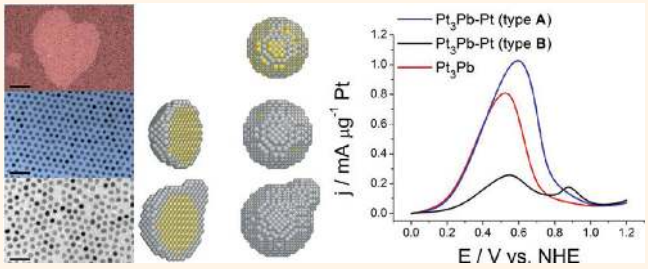

Formic acid is a promising chemical fuel for fuel cell applications. However, due to the dominance of the indirect reaction pathway and strong poisoning effects, the development of direct formic acid fuel cells has been impeded by the low activity of existing electrocatalysts at desirable operating voltage. We report the first synthesis of Pt_3Pb nanocrystals through solution phase synthesis and show they are highly efficient formic acid oxidation electrocatalysts. The activity can be further improved by manipulating the Pt_3Pb–Pt core–shell structure. Combined experimental and theoretical studies suggest that the high activity from Pt_3Pb and the Pt–Pb core–shell nanocrystals results from the elimination of CO poisoning and decreased barriers for the dehydrogenation steps. Therefore, the Pt_3Pb and Pt–Pb core–shell nanocrystals can improve the performance of direct formic acid fuel cells at desired operating voltage to enable their practical application.

KEYWORDS: platinum · lead · electrocatalysis · formic acid oxidation · core–shell · nanostructure · nanocrystal

Formic acid (FA), with high energy density (1740 Wh/kg, 2086 Wh/L) and easier storage and handling than H_2, is an attractive choice for chemical fuel in fuel cells, which could replace conventional batteries and at larger scale may possess higher efficiency than conventional combustion engines.[1−5] However, due to the dominance of the indirect reaction pathway and strong poisoning effects,[1,4,6] the development of direct formic acid fuel cells (DFAFCs) has been impeded by the low activity of existing electrocatalysts at desirable operating voltage (*i.e.*, at low oxidation potential). Various efforts have been made to improve the electrocatalyst for FA oxidation, including the use of adatoms[7−11] or making Pt-based alloys.[12−28]

Three possible reaction paths of FA oxidation have been proposed.[6,29−32]

$$HCOOH^* \rightarrow COOH^* + H^+ + e^- \rightarrow CO_2 + 2H^+ + 2e^- \quad \text{(i)}$$

$$HCOOH^* \rightarrow HCOO^* + H^+ + e^- \rightarrow CO_2 + 2H^+ + 2e^- \quad \text{(ii)}$$

$$HCOOH^* \rightarrow CO^* + H_2O \rightarrow CO_2 + 2H^+ + 2e^- \quad \text{(iii)}$$

Here, * represents an adsorbed state. Equation i is referred to as the direct pathway, where the removal of the first hydrogen atom from the C–H bond occurs to produce a hydroxy carbonyl, and then a second dehydrogenation step occurs at the O–H bond to produce CO_2. Equation ii is called the formate pathway, in which the dehydrogenation first occurs at the O–H bond to produce formate and then at the C–H bond to generate CO_2. Equation iii is known as the indirect pathway, in which CO* is produced by non-Faradaic dehydration of FA, then is further oxidized to CO_2. Both i and ii are accomplished by dehydrogenation (via different intermediates) to form CO_2 directly, so i and ii are sometimes referred to as a "direct pathway" jointly. Both experimental and computational results suggest that the dominance of the indirect reaction pathway, which generates the CO* poisoning intermediate, causes the problem of low activity at low oxidation potential. Pb has been identified as a promising adatom or alloying element to enhance FA

* Address correspondence to cbmurray@sas.upenn.edu.

Received for review January 23, 2012 and accepted March 2, 2012.

Published online March 02, 2012
10.1021/nn3003373

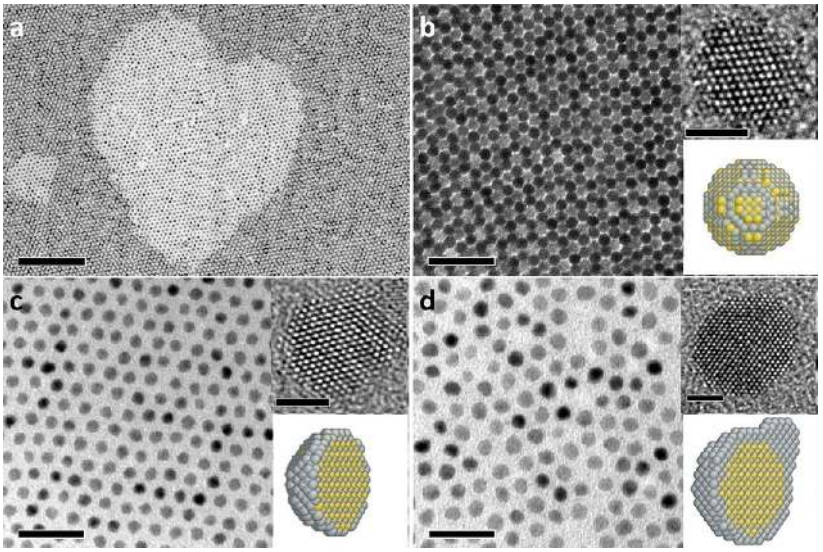

Figure 1. TEM images and (insets) HRTEM images of (a, b) Pt_3Pb NCs, (c) Pt_3Pb–Pt(type A) NCs, and (d) Pt_3Pb–Pt(type B) NCs. Scale bars: (a) 100 nm, (b, c, d) 20 nm, (insets) 2 nm.

oxidation activity and CO-poisoning tolerance of electrocatalysts.[15,18–21] Adding Pb into Pt electrocatalysts to enhance their activity has been demonstrated by both underpotential deposited Pb[33] and PtPb alloys made by high-temperature annealing,[15] as well as some Pt–Pb nanoparticles.[18–20,34–37] Here, we report the first synthesis of Pt_3Pb nanocrystals (NCs) and two types of core–shell structure based on such Pt_3Pb NCs through solution phase synthesis and show they are highly efficient FA oxidation electrocatalysts, particularly at desirable low oxidation potential. By combining the design and functional testing of novel Pt_3Pb, Pt_3Pb–Pt core–shell NCs of varying shell thickness and morphology with density functional theory (DFT) calculations, we have identified that the origin of the activity enhancement is the elimination of CO poisoning and a lowered activation barrier for the desirable direct reaction pathway.

RESULTS AND DISCUSSION

To synthesize Pt_3Pb NCs, Pt acetylacetonate [$Pt(acac)_2$] and Pb acetylacetonate [$Pb(acac)_2$] are dissolved in benzyl ether, oleic acid, oleylamine, and hexadecanethiol, and the reaction mixture is brought to 180 °C. The reducing agent, borane-triethylamine complex (BTEA), is injected into the reaction at 180 °C. After 30 min, Pt_3Pb NCs of 3.7 nm diameter ($\sigma < 5\%$) are purified and collected. Figure 1 shows the transmission electron microscope (TEM) images of the monodisperse Pt_3Pb NCs with a size of 3.7 nm ($\sigma < 5\%$). The interplanar distance measured from high resolution (HR) TEM is 2.34 Å (Figure S7), corresponding to the lattice spacing of the Pt_3Pb {111} planes. The TEM-deduced lattice constant is 4.05 Å, which is consistent with the values calculated from X-ray diffraction (XRD) data (4.08 Å) and DFT calculation (4.13 Å). The stoichiometry of Pt:Pb = 3:1 is confirmed by both energy dispersive X-ray spectroscopy (EDX) ($Pt_{76}Pb_{24}$, $\sigma < 5\%$) and inductively coupled plasma optical emission spectrometry (ICP-OES) ($Pt_{74.8}Pb_{25.2}$, $\sigma < 1\%$). Due to their extremely narrow size distribution, the Pt_3Pb NCs readily form large-area superlattices (Figures S7–9). The combination of long-chain carboxylic acid, amine, and thiol as the capping agent (stabilizer) is essential to the synthesis of Pt_3Pb NCs, although they can be substituted by similar ligands (Table S1). The synthesis in the absence of carboxylic acid and/or amine produces nanocrystals in a broad size distribution (Figures S3–5); in the absence of long-chain thiol, agglomerates are generated as the major product (Figure S6). The combination of hexadecylamine, adamantanecarboxylic acid, and hexadecanethiol produces nanorods in the PtPb phase, as reported by Yang *et al.*[34]

As it has been demonstrated that catalytic reactions could be sensitive to the morphology of the catalyst,[22,38–43] to better study the catalytic properties of Pt_3Pb, we prepare two more Pt–Pb core–shell nanostructures as control systems for comparison. We use the as-synthesized Pt_3Pb as seeds upon which to grow a second Pt layer. High-temperature growth facilitates the Pt precursor decomposition, inducing growth on any possible seed sites, usually forming islands as well as layers, while at lower temperature slower growth allows Pt to grow uniformly onto Pt_3Pb seeds at a low yield, forming an epitaxial layer. Figure 1c and d present the TEM images of these as-synthesized Pt_3Pb–Pt NCs. The size of Pt_3Pb–Pt NCs (here, we name them as "Pt_3Pb–Pt(type A)") by slow growth is 4.0 nm ($\sigma = 6\%$), slightly larger than the original Pt_3Pb NCs, while the size of Pt_3Pb–Pt NCs (here, we name them as "Pt_3Pb–Pt(type B)") by rapid growth is 4.9 nm ($\sigma > 10\%$) at broadened size distribution. Many Pt_3Pb–Pt(type B) NCs adopt an elongated morphology rather

than a uniform spherical morphology, indicating an island structure (Figures 2, S14). The monodisperse Pt_3Pb–Pt(type A) NCs form a large-area superlattice as readily as the original Pt_3Pb NCs (Figures S11, S12). Due to their broad size and shape distribution, Pt_3Pb–Pt(type B) NCs form only small-area superlattices (Figure S13). The composition of Pt:Pb = 83:17 (σ < 5%) for Pt_3Pb–Pt(type A) and Pt:Pb = 92:8 (σ < 5%) for Pt_3Pb–Pt(type B) is determined by both EDX and ICP-OES. The Pt:Pb ratio of a Pt_3Pb NC covered with a monolayer of Pt is calculated to be 82:18 (at a size of 4.0 nm), which is in good agreement with the Pt_3Pb–Pt(type A) composition. Figure 3 presents the EDX line scans of three types of Pt–Pb NCs. A Pt-rich shell for Pt_3Pb–Pt(type B) can be clearly seen as shown in the shadowed regions of Figure 3c. The difference between Pt_3Pb and Pt_3Pb–Pt(type A) is not apparent, because it is difficult for the equipped EDX detector to resolve the Pt shell as thin as a monolayer. As shown in Figure 4, the XRD pattern of Pt_3Pb–Pt(type A) is similar to Pt_3Pb with an fcc structure. Compared to Pt_3Pb and Pt_3Pb–Pt(type A), the XRD pattern of Pt_3Pb–Pt(type B) is shifted to a greater 2-theta angle (*i.e.*, smaller lattice constant), indicating a Pt-rich composition. Noting that the alloy phase could transform into an intermetallic phase upon annealing, we employ this phenomenon to investigate the composition and structure of these Pt–Pb NCs. After annealing at 600 °C for 30 min, the NC structures could be converted from the *A*1 phase to the ordered $L1_2$ phase ($AuCu_3$ structure), and phase segregation is observed (Figure 4). The major peaks of Pt_3Pb NCs fit the Pt_3Pb intermetallic phase. The trace impurity peaks are ascribed to the slight excess of Pt in the NCs. Pt_3Pb–Pt(type A) NCs show an increased amount of Pt, and the Pt_3Pb–Pt(type B) NCs exhibit even stronger signals for the pure Pt phase. These XRD data, with EDX and ICP-OES data and TEM images, support the claimed Pt–Pb structures and proposed mechanism of the Pt layer growth.

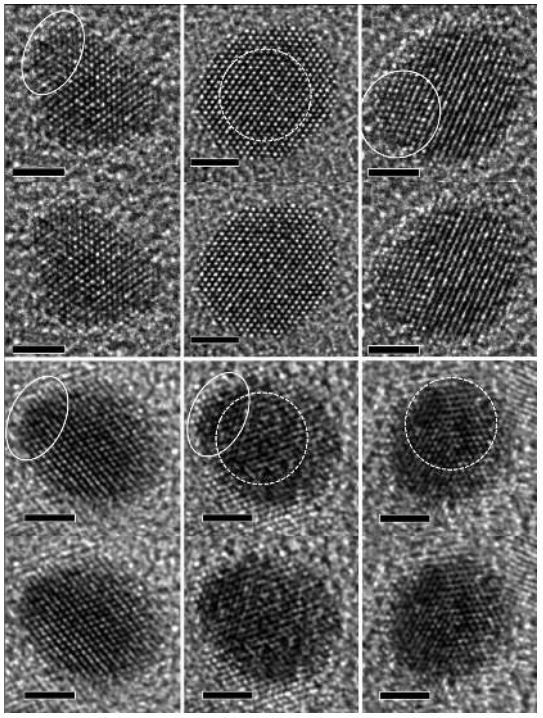

Figure 2. HRTEM images of Pt_3Pb–Pt(type B) nanocrystals. The circles represent the Pt_3Pb cores (dashed) and Pt islands (solid). For comparison purpose, exactly the same images but without circles are given below each circled image. Scale bars: 2 nm.

Figure 5a shows the electrochemical performance of Pt_3Pb NCs (treated by UV/ozone), compared to that of pure Pt (Pt black, Aldrich). As described earlier, FA oxidation on electrocatalysts follows both direct (including the formate pathway) and indirect pathways, corresponding to peak I and peak II in Figure 5a, respectively. The indirect pathway dominates the reactions on Pt catalysts, making the Pt unsuitable for DFAFC. However, on Pt_3Pb the direct pathway is more favorable, with little reaction occurring via the indirect pathway. At 0.3 V (typical anodic working voltage in DFAFC), the FA oxidation activity on Pt_3Pb is 33 times greater than that on Pt. Figure 5b presents a comparison of activities for the different Pt–Pb nanostructures. The Pt_3Pb–Pt(type A) NCs show the highest activity toward FA oxidation. The activity on Pt_3Pb–Pt(type B) NCs is much lower than that on the other two Pt–Pb nanostructures, while a peak at higher potential is observed, indicating FA oxidation on Pt_3Pb–Pt(type B) NCs does occur via the indirect pathway. It is worth noting that the Pt–Pb electrocatalysts demonstrated in Figure 5a and b are dense films (Figure S10) rather than supported catalysts. In a commercial fuel cell catalyst, ETEK Pt, Pt is supported on high surface area carbon (Vulcan-72R), which enables much higher catalyst utilization of ETEK Pt. To make the Pt–Pb electrocatalysts comparable to the commercial electrocatalysts, we load Pt–Pb NCs onto Vulcan-72R (Figure S15). The resulting

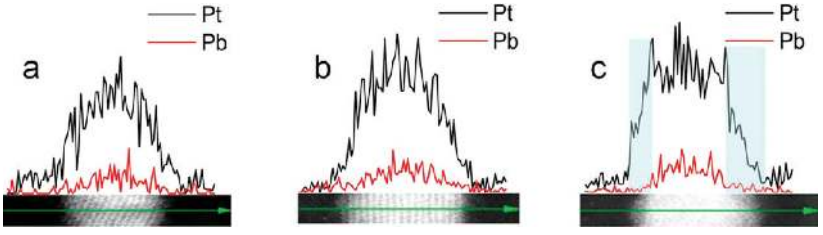

Figure 3. EDX line scans of (a) Pt_3Pb, (b) Pt_3Pb–Pt(type A), and (c) Pt_3Pb–Pt(type B) NCs.

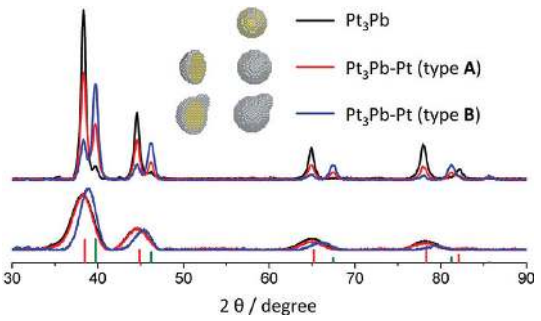

Figure 4. XRD patterns of (upper) annealed NCs and (lower) as-synthesized NCs. Index: (pink) Pt_3Pb, (green) Pt. Insets: models to represent Pt_3Pb–Pt nanostructures (yellow: Pb, gray: Pt).

Pt_3Pb/C and Pt_3Pb–Pt(type A)/C catalysts exhibit high activities, which are about 15 and 25 times (at 0.3 V) higher respectively than the corresponding activity of the commercial Pt/C catalyst (Figure 5c). Figure 6 shows *in situ* infrared reflection absorption spectra (IRRAS) of FA oxidation on different catalysts. The positive-going band at 2343 cm^{-1} is attributed to the asymmetric stretch vibration of CO_2, the product of FA oxidation. The band at around 2030 cm^{-1} is assigned to linear bound CO* (denoted as CO_L), the poison intermediate generated from the FA indirect pathway. The CO_L bands on Pt_3Pb–Pt(type B) NCs show a lower intensity compared to the ones generated from pure Pt, and no CO_L band is observed on both Pt_3Pb and Pt_3Pb–Pt(type A) NCs. The results suggest that FA oxidation occurs on Pt_3Pb or Pt_3Pb–Pt(type A) via the direct pathway and on Pt_3Pb–Pt(type B) or Pt black via the indirect pathway.

Apparent CO oxidation is observed neither in the polarization curves nor in the IRRAS spectra for both Pt_3Pb and Pt_3Pb–Pt(type A), because Pb alloying can relieve the CO-poisoning effect by weakening the adsorption strength of CO, as predicted in previous DFT calculations.[15,21] As a result, the FA oxidation activity increases at low potential due to the reduced CO poisoning. On the other hand, the low activity of Pt_3Pb–Pt(type B) NCs (but still better than pure Pt) can be explained by the structural relaxation of the Pt atoms deposited on Pt_3Pb NCs. According to XRD results (Figure 4), the Pt_3Pb–Pt(type B) NCs have a lattice constant close to pure Pt, smaller than lattice constants for Pt_3Pb NCs and Pt_3Pb–Pt(type A) NCs. Excess Pt atoms in Pt_3Pb–Pt(type B) NCs form thick Pt layers and Pt cluster islands on the Pt_3Pb core. These Pt thick layers and islands have similar electrocatalytic properties to pure Pt, which generates CO* from FA dehydration and decreases the overall activity. However, this mechanism cannot explain the further increase of total activity for Pt_3Pb–Pt(type A) NCs relative to Pt_3Pb NCs, since both of them have little CO-poisoning effect; thus there must be other factors causing the increase of the activity besides the avoidance of CO poisoning originated from Pb alloying.

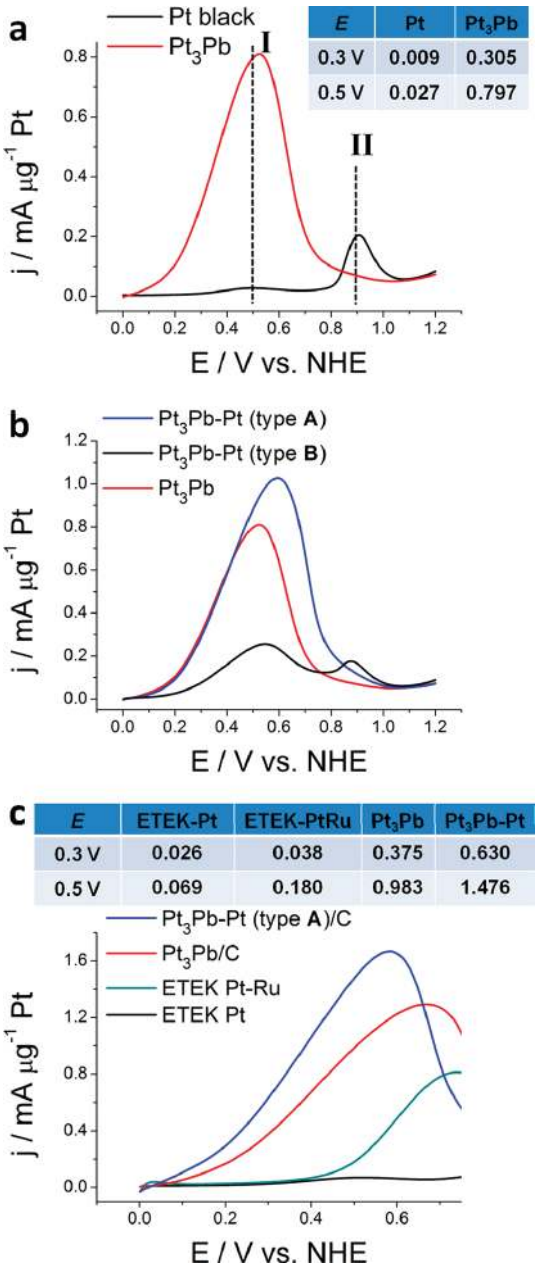

Figure 5. Polarization curves of (a) formic acid oxidation on Pt black and Pt_3Pb, (b) formic acid oxidation on Pt–Pb nanostructures, and (c) maximum activities of formic acid oxidation on carbon-supported catalysts. Tables in a and c present the activities (mA μg^{-1} Pt) of electrocatalysts at 0.3 and 0.5 V.

In order to understand physical mechanisms of activity enhancements on these Pt_3Pb NCs, we performed a series of DFT calculations to obtain the reaction energetics in different possible reaction paths on several model surfaces. The (111) surface is the most stable facet of the fcc lattice and contributes most of the area for the surface of bulk Pt and alloy, as well as most of the NCs. Here, pure Pt NCs are simulated by a Pt(111) surface; Pt_3Pb NCs are simulated by a (111) surface of Pt_3Pb crystal; Pt_3Pb–Pt(type A) NCs are simulated by the Pt_3Pb(111) surface with the top layer

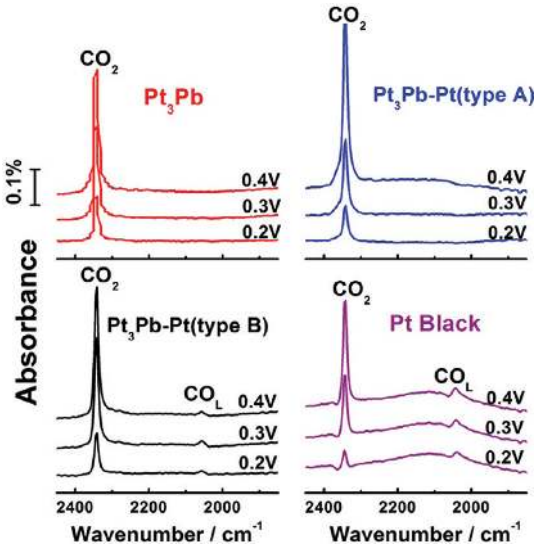

Figure 6. ***In situ*** **IRRAS spectra for formic acid oxidation on Pt−Pb nanostructures and Pt black.**

as pure Pt, labeled as $Pt_3PbPt(111)$, as shown in Figure 7a. Lattice constants of Pt and Pt_3Pb obtained from DFT calculations are 3.98 and 4.13 Å, respectively. Both the direct path and formate path are explored on these surfaces as follows: (i) direct pathway: HCOOH → HCOOH* → COOH* + H* → CO_2 + 2H*; (ii) formate pathway: HCOOH → HCOOH* → HCOO* + H* → CO_2 + 2H*. Here we use these surface reactions under ultrahigh-vacuum (UHV) conditions to simulate the corresponding electrochemical reactions, which is a general procedure to qualitatively describe the activities of electrocatalysts.[44,45]

The reaction and activation energies for all elementary steps in both pathways on these three types of model surfaces are listed in Figure 7b, c, and d, respectively. On the Pt (111) surface, the first dehydrogenation step in the formate pathway has almost the same activation barrier as the direct pathway (0.71 eV), indicating a significant proportion of HCOOH* may first lose the hydrogen atom connected to the oxygen atom; however, the formate pathway has a much higher activation barrier than the direct pathway for the second dehydrogenation step (1.23 *vs* 0.71 eV). Thus, even without CO poisoning, the total reaction rate may be impeded by the stable formate intermediate occupying a large fraction of active sites on the surface.[30,32] On the $Pt_3Pb(111)$ surface, all the activation barriers are decreased in comparison with Pt(111), indicating that the total activity of FA oxidation may increase. However, the activation barrier for the first dehydrogenation step in the direct pathway is much higher than its counterpart in the formate pathway (0.57 *vs* 0.36 eV), which means formate "poisoning" could become worse on the $Pt_3Pb(111)$ surface. Finally, for the $Pt_3PbPt(111)$ surface, there are two types of Pt atoms on the top Pt layer: type 1 [without Pb as nearest neighbor ($NN_{Pb} = 0$)] and type 2 [with one Pb as nearest neighbor ($NN_{Pb} = 1$)], and type 1 has a stronger adsorption strength for reaction intermediates than type 2. The paths are found to have the lowest activation barriers when carbon-related intermediates (HCOOH*, COOH*, HCOO*) are adsorbed on a type 2 atom and H atoms are adsorbed on type 1 atoms. In these paths, the dehydrogenation steps for both direct and formate pathways have comparable activation barriers (0.58 *vs* 0.55 eV), much smaller than those on Pt(111), which means that the formate "poisoning" effect on the $Pt_3PbPt(111)$ surface is much smaller than on the $Pt_3Pb(111)$ surface. For the second dehydrogenation step in the direct pathway, the dehydrogenation barrier is also smaller than that on the $Pt_3Pb(111)$ surface (0.56 eV), so this path has the smallest maximum barrier on these investigated surfaces. In addition, as shown in Figure 7b−d, the adsorption strengths of HCOOH on $Pt_3PbPt(111)$ increase compared with Pt(111) and $Pt_3Pb(111)$ surfaces. Because the adsorption energy of HCOOH is relatively weak compared with those of typical small molecules, such as H_2 and O_2 and is even comparable with H_2O (≈ -0.2 eV), a stronger adsorption strength may increase the coverage of HCOOH* on catalyst surfaces for the following reaction steps.

In summary, combined experimental and theoretical studies show that the increased activity for Pt_3Pb NCs and Pt_3Pb−Pt(type A) NCs relative to Pt NCs results from the elimination of CO poisoning and decreased barriers for dehydrogenation steps. The further increase of activity for Pt_3Pb−Pt(type A) NCs relative to Pt_3Pb NCs may result from continuous decreases of dehydrogenation barriers, strong adsorption of reactant molecules, and, most importantly, the suppression of the formate path and avoidance of stable formate intermediates. However, the overall activity decreases with further increase of the Pt ratio due to CO* poisoning caused by structural relaxation of the extra Pt atoms. Thus, both the existence and thickness of the Pt shell surrounding the Pt_3Pb NCs are critical to achieve high reaction rate, reinforcing the notion that even materials with very similar chemical compositions can be manipulated by control of nanoscale structures to obtain high catalytic activities.

METHODS

Synthesis. Pt_3Pb NCs: Under a nitrogen flow, 0.2 g of $Pt(acac)_2$ and 0.2 g of $Pb(acac)_2$ are dissolved in 5 mL of benzyl ether, 18.4 mL of oleylamine, 3.2 mL of oleic acid, and 11.1 mL of 1-hexadecanethiol. The formed solution is dipped into an oil bath that is preheated to 180 °C. Once the temperature of the solution in the reaction flask reaches 180 °C, 0.46 mL of borane-triethylamine complex is injected into the reaction flask. The

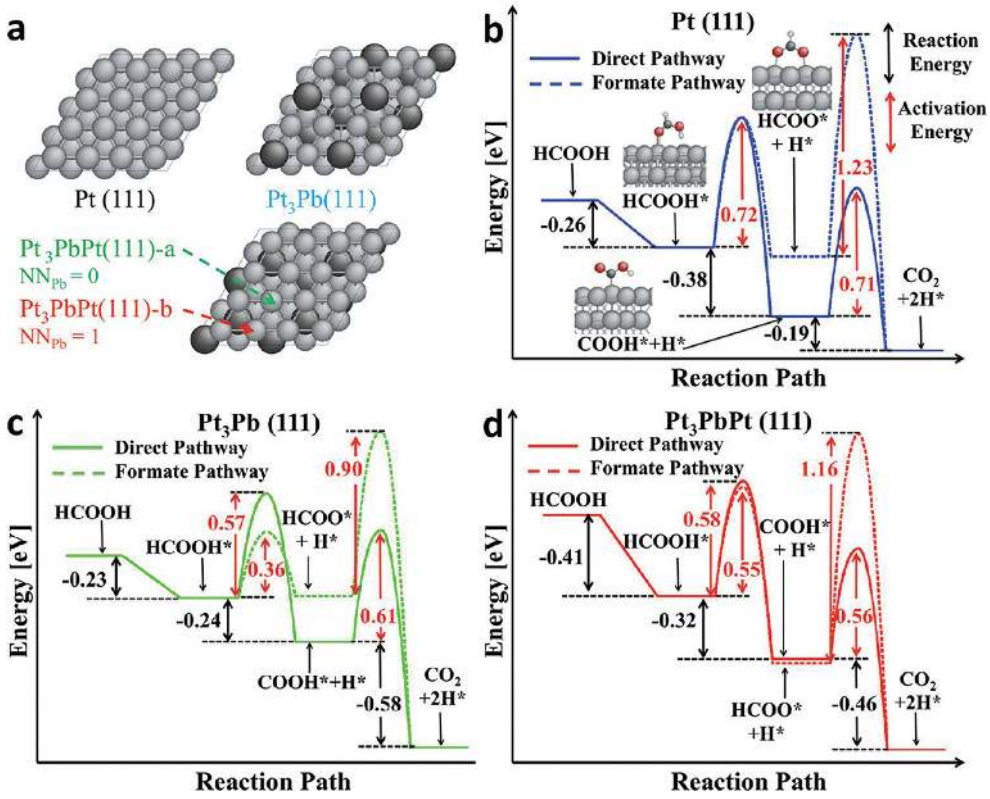

Figure 7. (a) Surface models of Pt(111), Pt_3Pb(111), and Pt_3Pb−Pt(111) atoms. Gray (black) stands for Pt (Pb) atoms. (b, c, d) Reaction pathways of HCOOH → CO_2 + 2H* with reaction/activation energies of elementary steps on different model surfaces. Here the final product H* is located at the most stable adsorption site on the corresponding surface; thus three surfaces have different total reaction energies because of different H adsorption strengths.

temperature is kept at 180 °C for 30 min after the injection. After reaction, the solution is allowed to cool. The product is precipitated by ethanol and then is redispersed in hexane. The hexane solution is further purified by centrifuge at 50 000 rpm (Thermo, WX Ultra 100). As the regular size-selective precipitation does not work well for the purification process because the byproducts and impurities (mainly Pb-based compounds) have very similar properties of solubility to the Pt_3Pb NCs, the high-speed centrifuge is necessary to obtain pure Pt_3Pb NCs, as shown in Figure S2. **Pt_3Pb−Pt(type A) NCs:** 0.02 g (estimated based on ICP-OES data) of Pt_3Pb NCs, 0.02 g of $Pt(acac)_2$, and 0.026 g of 1,2-hexadecanediol are dissolved in 5 mL of benzyl ether, 3.68 mL of oleylamine, and 0.63 mL of oleic acid. The formed solution is slowly (5−10 °C/min) heated to 200 °C and is kept at 200 °C for 30 min. After reaction, the solution is allowed to cool. The product is washed by hexane/ethanol. **Pt_3Pb−Pt(type B) NCs:** 0.02 g of $Pt(acac)_2$ and 0.026 g of 1,2-hexadecanediol are dissolved in 5 mL of benzyl ether, 3.68 mL of oleylamine, and 0.63 mL of oleic acid. The formed solution is rapidly heated to 180 °C. Once the temperature of the solution in the reaction flask reaches 180 °C, 0.02 g (estimated based on ICP-OES data) of Pt_3Pb NC/1 mL hexane solution is injected into the reaction flask. The reaction is further brought to 200 °C and is kept at 200 °C for 30 min. After the reaction, the solution is allowed to cool. The product is washed by hexane/ethanol.

Characterizations. TEM images are taken on a JEOL1400 TEM at 120 kV. The HRTEM image and EDX data are taken on a JEOL2010F TEM at 200 kV. Partial HRTEM images (insets of Figure 1) are taken using a Cs-corrected FEI Titan 80-300 at 300 kV, with the aberration corrector tuned to a flat phase region of >20 mrad (<0.1 nm information transfer), leaving a residual spherical aberration of <1.5 μm. SEM images are taken on a JEOL JSM7600F. The HR scanning transmission electron microscope (STEM) images are taken using a Hitachi HD2700C dedicated 200 kV cold emission STEM. XRD patterns are obtained on a Rigaku Smartlab diffractometer with Cu Kα radiation (λ = 1.5418 Å). Quantitative elemental analyses for the composition of NCs are carried out with both EDX and inductively coupled plasma optical emission spectrometry on a SPECTRO GENESIS ICP spectrometer.

Electrochemical Measurements. Electrochemical measurements are performed on a potentiostat (Epsilon, Bioanalytical Systems Inc.). An Ag/AgCl electrode is used as a reference electrode, and a platinum coil is used as the counter electrode. All potentials are converted to values with reference to a normal hydrogen electrode (NHE). The electrolyte is 0.1 M sulfuric acid. All water used in the experiments is Millipore ultrapure water (18.2 MΩ). Working electrodes are prepared by dropping the NC solution (in hexane, the concentration has been determined by ICP-OES) onto glassy carbon. The electrodes covered with NC thin films are then treated by UV/ozone for 24 h before measurement. Pt_3Pb/C catalysts are treated by plasma (O_2, 100 W, 30 min) and thermal treatment (4% H_2 argon balanced, 600 °C, 30 min) for the best performance. Pt_3Pb−Pt(type A)/C catalysts are treated by thermal treatment (air, 210 °C, 30 min, temperature reduced in order to retain the core−shell morphologies; 4% H_2 argon balanced, 210 °C, 30 min). All measurements are carried out at room temperature in 0.1 M H_2SO_4 + 0.5 M FA at a sweep rate of 20 mV/s. The third sweeps are recorded. For carbon-supported catalysts, the sweep with maximum activity is recorded. The rotating disk electrode (900 rpm) is used for carbon-supported catalysts to suppress the gas formation during reactions.

IRRAS Measurements. *In situ* IRRAS studies are carried out with a Nicolet Nexus 670 Fourier-transform infrared spectrometer equipped with a mercury cadmium telluride detector cooled with liquid nitrogen. An unpolarized light beam is used. The spectral resolution is set to 8 cm^{-1}, and 128 interferograms are together added to each spectrum. Spectra are given in absorbance units defined as $A = -\log(R/R_0)$, where R and R_0 represent the reflected infrared intensities corresponding to the sample and reference single-beam spectrum, respectively. The reference spectrum is collected at 0.005 V. All spectra are collected in a solution of 0.1 M formic acid and 0.1 M sulfuric acid. The nanocrystals are placed on Au(111) surfaces to ensure a good

current collection and reflectivity. A ZnSe hemisphere is used as the infrared window.

DFT Calculation Procedures. All DFT calculations are performed by using the Vienna *ab initio* simulation package (VASP).[46] We use projector augmented wave (PAW) potentials[47] with Perdew–Burke–Ernzerhof (PBE) exchange–correlation functional[48] in non-spin-polarized condition, because all the adsorbed intermediates are found to be at nonmagnetic states. All (111) surfaces are modeled by (4 × 2) supercells with four-layer slabs (8 atoms per layer), where the top two layers are fully relaxed and the vacuum size is larger than 15 Å. A Monkhorst–Pack k-point of 3 × 5 × 1 grids is applied for Brillouin-zone integration. Partial occupancies of eigenstates are determined by first-order Methfessel–Paxton smearing of σ = 0.2 eV. The cut-off energy for plane wave basis is 400 eV. The minimum energy path of each dehydrogenation step is searched by the climbing image nudged elastic band (CI-NEB) method integrated in VASP.[49]

Conflict of Interest: The authors declare no competing financial interest.

Acknowledgment. C.B.M. and Y.J.K. acknowledge partial support from the U.S. Army Research Office (ARO) under award number MURI W911NF-08-1-0364. Y.J.K.'s development of catalytic NCs was partially supported by the Nano/Bio Interface Center through the National Science Foundation NSEC DMR08-32802. C.B.M. thanks the Richard Perry University Professorship for the support of his supervisor role. L.Q. and J.L. acknowledge support by NSF grant DMR-1120901 and AFOSR grant FA9550-08-1-0325. Research was carried out in part at the Center for Functional Nanomaterials (CFN) and Department of Chemistry, Brookhaven National Laboratory (BNL), which is supported by the U.S. Department of Energy, Office of Basic Energy Sciences, under Contract No. DE-AC02-98CH10886. We thank Charles Black and Fernando Camino at CFN for their assistance, Jin-Yi Wang at Fudan University for valuable discussion, and David Vann at Department of Earth and Environmental Science (University of Pennsylvania) for assistance in ICP-OES.

Supporting Information Available: This material is available free of charge via the Internet at http://pubs.acs.org.

REFERENCES AND NOTES

1. Rice, C.; Ha, R. I.; Masel, R. I.; Waszczuk, P.; Wieckowski, A.; Barnard, T. Direct Formic Acid Fuel Cells. *J. Power Sources* **2002**, *111*, 83–89.
2. Winter, M.; Brodd, R. J. What are Batteries, Fuel Cells, and Supercapacitors? *Chem. Rev.* **2004**, *104*, 4245–4269.
3. Haile, S. M. Fuel Cell Materials and Components. *Acta Mater.* **2003**, *51*, 5981–6000.
4. Rice, C.; Ha, S.; Masel, R. I.; Wieckowski, A. Catalysts for Direct Formic Acid Fuel Cells. *J. Power Sources* **2003**, *115*, 229–235.
5. Mazumder, V.; Lee, Y.; Sun, S. H. Recent Development of Active Nanoparticle Catalysts for Fuel Cell Reactions. *Adv. Funct. Mater.* **2010**, *20*, 1224–1231.
6. Capon, A.; Parsons, R. Oxidation of Formic-Acid at Noble-Metal Electrodes Part 3. Intermediates and Mechanism on Platinum-Electrodes. *J. Electroanal. Chem.* **1973**, *45*, 205–231.
7. Adzic, R. R.; Simic, D. N.; Despic, A. R.; Drazic, D. M. Electrocatalysis by Foreign Metal Monolayers–Oxidation of Formic-Acid on Platinum. *J. Electroanal. Chem.* **1975**, *65*, 587–601.
8. Adzic, R. R.; Simic, D. N.; Despic, A. R.; Drazic, D. M. Electrochemical Oxidation of Formic-Acid at Noble-Metals–Catalytic Effects of Foreign Metal Monolayers. *J. Electroanal. Chem.* **1977**, *80*, 81–99.
9. Adzic, R. R.; Tripkovic, A. V.; Markovic, N. M. Structural Effects in Electrocatalysis–Oxidation of Formic-Acid and Oxygen Reduction on Single-Crystal Electrodes and the Effects of Foreign Metal Adatoms. *J. Electroanal. Chem.* **1983**, *150*, 79–88.
10. Watanabe, M.; Furuuchi, Y.; Motoo, S. Electrocatalysis by Ad-atoms. 13. Preparation of Ad-Electrodes with Tin Ad-atoms for Methanol, Formaldehyde and Formic-Acid Fuel-Cells. *J. Electroanal. Chem.* **1985**, *191*, 367–375.
11. Schmidt, T. J.; Behm, R. J.; Grgur, B. N.; Markovic, N. M.; Ross, P. N. Formic Acid Oxidation on Pure and Bi-modified Pt(111): Temperature Effects. *Langmuir* **2000**, *16*, 8159–8166.
12. Sun, S. G.; Clavilier, J.; Bewick, A. The Mechanism of Electrocatalytic Oxidation of Formic-Acid on Pt (100) and Pt (111) in Sulfuric-Acid Solution–An EMIRS Study. *J. Electroanal. Chem.* **1988**, *240*, 147–159.
13. Markovic, N. M.; Gasteiger, H. A.; Ross, P. N.; Jiang, X. D.; Villegas, I.; Weaver, M. J. Electrooxidation Mechanisms of Methanol and Formic-Acid on Pt-Ru Alloys Surfaces. *Electrochim. Acta* **1995**, *40*, 91–98.
14. Sun, S. H.; Murray, C. B.; Weller, D.; Folks, L.; Moser, A. Monodisperse FePt Nanoparticles and Ferromagnetic FePt Nanocrystal Superlattices. *Science* **2000**, *287*, 1989–1992.
15. Casado-Rivera, E.; Volpe, D. J.; Alden, L.; Lind, C.; Downie, C.; Vazquez-Alvarez, T.; Angelo, A. C. D.; DiSalvo, F. J.; Abruna, H. D. Electrocatalytic Activity of Ordered Intermetallic Phases for Fuel Cell Applications. *J. Am. Chem. Soc.* **2004**, *126*, 4043–4049.
16. Greeley, J.; Mavrikakis, M. Alloy Catalysts Designed from First Principles. *Nat. Mater.* **2004**, *3*, 810–815.
17. Schaak, R. E.; Sra, A. K.; Leonard, B. M.; Cable, R. E.; Bauer, J. C.; Han, Y. F.; Means, J.; Teizer, W.; Vasquez, Y.; Funck, E. S. Metallurgy in a Beaker: Nanoparticle Toolkit for the Rapid Low-Temperature Solution Synthesis of Functional Multimetallic Solid-state Materials. *J. Am. Chem. Soc.* **2005**, *127*, 3506–3515.
18. Alden, L. R.; Han, D. K.; Matsumoto, F.; Abruna, H. D.; DiSalvo, F. J. Intermetallic PtPb Nanoparticles Prepared by Sodium Naphthalide Reduction of Metal-organic Precursors: Electrocatalytic Oxidation of Formic Acid. *Chem. Mater.* **2006**, *18*, 5591–5596.
19. Zhang, L. J.; Wang, Z. Y.; Xia, D. G. Bimetallic PtPb for Formic Acid Electro-oxidation. *J. Alloys Compd.* **2006**, *426*, 268–271.
20. Liu, Z. L.; Guo, B.; Tay, S. W.; Hong, L.; Zhang, X. H. Physical and Electrochemical Characterizations of PtPb/C Catalyst Prepared by Pyrolysis of Platinum(II) and Lead(II) Acetylacetonate. *J. Power Sources* **2008**, *184*, 16–22.
21. Wang, L. L.; Johnson, D. D. Electrocatalytic Properties of PtBi and PtPb Intermetallic Line Compounds via DFT: CO and H Adsorption. *J. Phys. Chem. C* **2008**, *112*, 8266–8275.
22. Kang, Y. J.; Murray, C. B. Synthesis and Electrocatalytic Properties of Cubic Mn-Pt Nanocrystals (Nanocubes). *J. Am. Chem. Soc.* **2010**, *132*, 7568–7569.
23. Peng, Z. M.; Yang, H. PtAu Bimetallic Heteronanostructures Made by Post-Synthesis Modification of Pt-on-Au Nanoparticles. *Nano Res.* **2009**, *2*, 406–415.
24. Peng, Z. M.; Yang, H. Designer Platinum Nanoparticles: Control of Shape, Composition in Alloy, Nanostructure and Electrocatalytic Property. *Nano Today* **2009**, *4*, 143–164.
25. Lee, H. J.; Habas, S. E.; Somorjai, G. A.; Yang, P. D. Localized Pd Overgrowth on Cubic Pt Nanocrystals for Enhanced Electrocatalytic Oxidation of Formic Acid. *J. Am. Chem. Soc.* **2008**, *130*, 5406–5407.
26. Arenz, M.; Stamenkovic, V.; Schmidt, T. J.; Wandelt, K.; Ross, P. N.; Markovic, N. M. The Electro-oxidation of Formic Acid on Pt-Pd Single Crystal Bimetallic Surfaces. *Phys. Chem. Chem. Phys.* **2003**, *5*, 4242–4251.
27. Ji, X. L.; Lee, K. T.; Holden, R.; Zhang, L.; Zhang, J. J.; Botton, G. A.; Couillard, M.; Nazar, L. F. Nanocrystalline Intermetallics on Mesoporous Carbon for Direct Formic Acid Fuel Cell Anodes. *Nat. Chem.* **2010**, *2*, 286–293.
28. Bauer, J. C.; Chen, X.; Liu, Q. S.; Phan, T. H.; Schaak, R. E. Converting Nanocrystalline Metals into Alloys and Intermetallic Compounds for Applications in Catalysis. *J. Mater. Chem.* **2008**, *18*, 275–282.
29. Samjeske, G.; Miki, A.; Ye, S.; Yamakata, A.; Mukouyama, Y.; Okamoto, H.; Osawa, M. Potential Oscillations in Galvanostatic Electrooxidation of Formic Acid on Platinum: A Time-Resolved Surface-Enhanced Infrared Study. *J. Phys. Chem. B* **2005**, *109*, 23509–23516.

30. Chen, Y. X.; Heinen, M.; Jusys, Z.; Behm, R. J. Bridge-Bonded Formate: Active Intermediate or Spectator Species in Formic Acid Oxidation on a Pt Film Electrode? *Langmuir* **2006**, *22*, 10399–10408.
31. Samjeske, G.; Miki, A.; Ye, S.; Osawa, M. Mechanistic Study of Electrocatalytic Oxidation of Formic Acid at Platinum in Acidic Solution by Time-Resolved Surface-Enhanced Infrared Absorption Spectroscopy. *J. Phys. Chem. B* **2006**, *110*, 16559–16566.
32. Neurock, M.; Janik, M.; Wieckowski, A.; First, A Principles Comparison of the Mechanism and Site Requirements for the Electrocatalytic Oxidation of Methanol and Formic Acid over Pt. *Faraday Discuss.* **2008**, *140*, 363–378.
33. Xia, X. H.; Iwasita, T. Influence of Underpotential Deposited Lead upon the Oxidation of HCOOH in $HClO_4$ at Pt-electrodes. *J. Electrochem. Soc.* **1993**, *140*, 2559–2565.
34. Maksimuk, S.; Yang, S. C.; Peng, Z. M.; Yang, H. Synthesis and Characterization of Ordered Intermetallic PtPb Nanorods. *J. Am. Chem. Soc.* **2007**, *129*, 8684–8685.
35. Roychowdhury, C.; Matsumoto, F.; Zeldovich, V. B.; Warren, S. C.; Mutolo, P. F.; Ballesteros, M.; Wiesner, U.; Abruna, H. D.; DiSalvo, F. J. Synthesis, Characterization, and Electrocatalytic Activity of PtBi and PtPb Nanoparticles Prepared by Borohydride Reduction in Methanol. *Chem. Mater.* **2006**, *18*, 3365–3372.
36. Matsumoto, F.; Roychowdhury, C.; DiSalvo, F. J.; Abruna, H. D. Electrocatalytic Activity of Ordered Intermetallic PtPb Nanoparticles Prepared by Borohydride Reduction toward Formic Acid Oxidation. *J. Electrochem. Soc.* **2008**, *155*, B148–B154.
37. Alden, L. R.; Roychowdhury, C.; Matsumoto, F.; Han, D. K.; Zeldovich, V. B.; Abruna, H. D.; DiSalvo, F. J. Synthesis, Characterization, and Electrocatalytic Activity of PtPb Nanoparticles Prepared by Two Synthetic Approaches. *Langmuir* **2006**, *22*, 10465–10471.
38. Wang, D. Y.; Kang, Y. J.; Doan-Nguyen, V.; Chen, J.; Kungas, R.; Wieder, N. L.; Bakhmutsky, K.; Gorte, R. J.; Murray, C. B. Synthesis and Oxygen Storage Capacity of Two-Dimensional Ceria Nanocrystals. *Angew. Chem., Int. Ed.* **2011**, *50*, 4378–4381.
39. Alayoglu, S.; Nilekar, A. U.; Mavrikakis, M.; Eichhorn, B. Ru-Pt Core-Shell Nanoparticles for Preferential Oxidation of Carbon Monoxide in Hydrogen. *Nat. Mater.* **2008**, *7*, 333–338.
40. Liu, Z. F.; Jackson, G. S.; Eichhorn, B. W. Intermetallic PtSn Core-Shell, and Alloy Nanoparticles as CO-Tolerant Electrocatalysts for H_2 Oxidation. *Angew. Chem., Int. Ed.* **2010**, *49*, 3173–3176.
41. Habas, S. E.; Lee, H.; Radmilovic, V.; Somorjai, G. A.; Yang, P. Shaping Binary Metal Nanocrystals through Epitaxial Seeded Growth. *Nat. Mater.* **2007**, *6*, 692–697.
42. Bratlie, K. M.; Lee, H.; Komvopoulos, K.; Yang, P. D.; Somorjai, G. A. Platinum Nanoparticle Shape Effects on Benzene Hydrogenation Selectivity. *Nano Lett.* **2007**, *7*, 3097–3101.
43. Lee, I.; Delbecq, F.; Morales, R.; Albiter, M. A.; Zaera, F. Tuning Selectivity in Catalysis by Controlling Particle Shape. *Nat. Mater.* **2009**, *8*, 132–138.
44. Hammer, B.; Norskov, J. K. Theoretical Surface Science and Catalysis—Calculations and Concepts. *Adv. Catal.* **2000**, *45*, 71–129.
45. Kowal, A.; Li, M.; Shao, M.; Sasaki, K.; Vukmirovic, M. B.; Zhang, J.; Marinkovic, N. S.; Liu, P.; Frenkel, A. I.; Adzic, R. R. Ternary Pt/Rh/SnO_2 Electrocatalysts for Oxidizing Ethanol to CO_2. *Nat. Mater.* **2009**, *8*, 325–330.
46. Kresse, G.; Furthmüller, J. Efficient Iterative Schemes for ab initio Total-Energy Calculations using a Plane-Wave Basis Set. *Phys. Rev. B* **1996**, *54*, 11169–11186.
47. Blochl, P. E. Projector Augmented-Wave Method. *Phys. Rev. B* **1994**, *50*, 17953–17979.
48. Perdew, J. P.; Burke, K.; Ernzerhof, M. Generalized Gradient Approximation Made Simple. *Phys. Rev. Lett.* **1996**, *77*, 3865–3868.
49. Henkelman, G.; Uberuaga, B. P.; Jonsson, H. A Climbing Image Nudged Elastic Band Method for Finding Saddle Points and Minimum Energy Paths. *J. Chem. Phys.* **2000**, *113*, 9901–9904.